Supplementary materials

Ce-doped Ni-S nanosheets on Ni foam supported NiMoO$_4$ micropillars: Fast electrodepostion, improved electrocatalytic activity and ultralong durability for oxygen evolution reaction in various electrolytes

Fangfang Wang, Zihao Liu, Kuanjian Zhang, Qingqing Zha and Yonghong Ni*

College of Chemistry and Materials Science, Key Laboratory of Functional Molecular Solids, Ministry of Education, Anhui Provincial Engineering Laboratory for New-Energy Vehicle Battery Energy-Storage Materials, Anhui Normal University, 189 Jiuhua Southern Road, Wuhu, 241002, PR China. Fax: +86-553-3869303. niyh@mail.ahnu.edu.cn (Y. H. Ni)

Characterizations

The phases of the products were characterized by the X-ray powder diffraction technology. The data were collected on a Bruker D8 X-ray diffractometer equipped with Cu Kα radiation (λ = 0.154060 nm), employing a scanning rate of 0.2° s^{-1} and a 2θ range from 10° to 80°. The morphology and elemental composition of the products were characterized on a Hitachi Regulus-8100 field emission scanning electron microscope (FESEM) equipped with an energy dispersive X-ray analyzer, employing operated voltages of 15 kV (for Mapping). Transmission electron microscopy (TEM) images were obtained on a HT7700 transmission electron microscope with an accelerating voltage of 120 kV. X-ray photoelectron spectroscopy was employed to analyze the chemical state and composition of the samples, which was carried out on an ESCALAB 250

instrument with a monochromatic Al Kα (hν = 1486.6 eV). The inductively coupled plasma mass-spectroscopy (ICP-MS) was employed to analyze the composition of Ni, Mo, Ce and S. N_2 adsorption−desorption experiments and pore size distribution were used for measuring the specific surface area of the sample by the method of Brunauer−Emmett−Teller (BET). Operando Raman measurements were recorded using a Raman spectrometer (RENISHAW inVia system, U.K.) with a 532 nm He/Ne laser as the excitation source. To avoid the interference of Ni substrate during characterizations, the final product was peeled off from Ni foam.

Electrochemical measurements

All electrochemical tests in this paper were performed on the CHI660E (Chenhua, China) electrochemical workstation with a typical three-electrode system at room temperature. The as-prepared catalysts/NF (1 cm × 1 cm), a graphite rod, and an Hg/HgO electrodes were used as the working electrode, the counter electrode, and the reference electrode, respectively. All potentials measured were calibrated to the reversible hydrogen electrode (RHE) according to the Nernst equation: $E_{RHE} = E_{Hg/HgO} + 0.059 \times pH + 0.098$. Before the electrochemical test, the working electrode was pretreated by cyclic voltammetry (CV) at the scan rate of 100 mV s^{-1} until steady state. The polarization curves were measured in different electrolytes by linear sweep voltammetry (LSV) at a scan rate of 1 mV s^{-1} with the 85% iR compensation. Electrochemical impedance spectroscopy (EIS) measurements were performed at the open circuit voltage in the frequency range of 0.01 Hz−10 kHz with amplitude of 5 mV AC amplitude. The electrochemically active surface area (ECSA) was estimated by testing the double-layer capacitance (C_{dl}) based on the linear relation between ECSA and C_{dl}. To obtain the C_{dl} value, CV curves in a non-Faradaic region were measured at a potential window from 0.877 to 0.977 V (vs RHE) with the scan rates

of 20, 40, 60, 80, and 100 mV s^{-1}, respectively. Subsequently, a linear relation between Δj (= $j_{anodic} - j_{cathodic}$)/2 at the potential of 0.927 V and the scan rate for each CV was plotted. ECSA-normalized LSV curves were calculated through the equation: $j_{ECSA} = j/C_{dl}$.

The turnover frequency (TOF) value was calculated based on the current density from the equation [1]:

$$TOF = (j \times N_A)/(n \times \tau \times F) \qquad (1)$$

Where j (A) is the current density during the LSV test in 1 M KOH at a certain voltage; N_A is the Avogadro number (6.02×10^{23} mol^{-1}); n is the number of electrons transferred (for OER, n = 4); F is the Faraday constant (96485 C mol^{-1}); and τ is the surface concentration of active sites or the number of participating atoms in the catalyst material.

The number of active sites involved in OER was determined based on the redox peak method [2]. We used the backward reduction peak to calculate the number of active sites. The CV curve was record at scan rate of 1 mV s^{-1}. The τ value was calculated by the below equation:

$$\tau = S/(V \times q) \qquad (2)$$

Where S (V · A) is integral area from CV reduction peak (because the area of the oxidation peak and the one of the reduction peak are the same, the reduction peak is selected for the area fitting here.) and the V is the scan rate (= 1 mV s^{-1}), q is 1.602×10^{-19} C (the charge of a single electron).

The Faradaic efficiency (FE) of CeNiS@NiMoO$_4$/NF electrode was obtained by comparing the actual gas content during electrolysis with the theoretical value.

The durability was evaluated by comparing LSV curves before and after CV cycling test and chronopotentiometry in different electrolytes.

The overall water splitting performance without iR compensation was implemented in 1 M KOH

solution. The two-electrode device was assembled with the prepared integral electrode and Pt/C/NF as the anode and cathode, respectively. The water splitting performances of the (-)Pt/C/NF || IrO_2/NF(+) electrodes were also measured as a control. The polarization curve was carried out under the potential window of 1.2-1.8 V with the scan rate of 5 mV s^{-1}. The stability was assessed through the chronopotentiometry at 20 mA cm^{-2}.

In addition, it has been reported previously in the literature that iron impurities contained in the electrolyte could affect the overpotential of the catalysts for OER [2,3]. In this work, KOH solution has been treated with the highly pure $Ni(OH)_2$ to absorb Fe impurities in the electrolytes before OER tests in the light of previous reports [2,3].
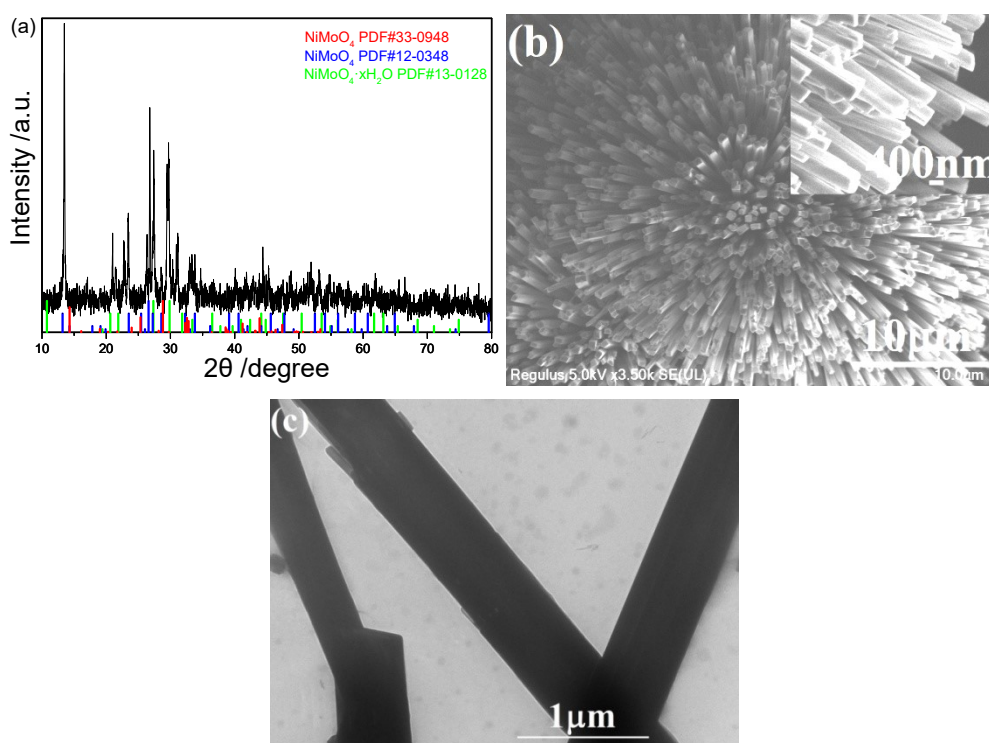
Figure S1. (a) XRD pattern, (b) FESEM and (c) TEM images of the as-obtained $NiMoO_4$ precursor. The inset in (b) is a high magnification FESEM image.
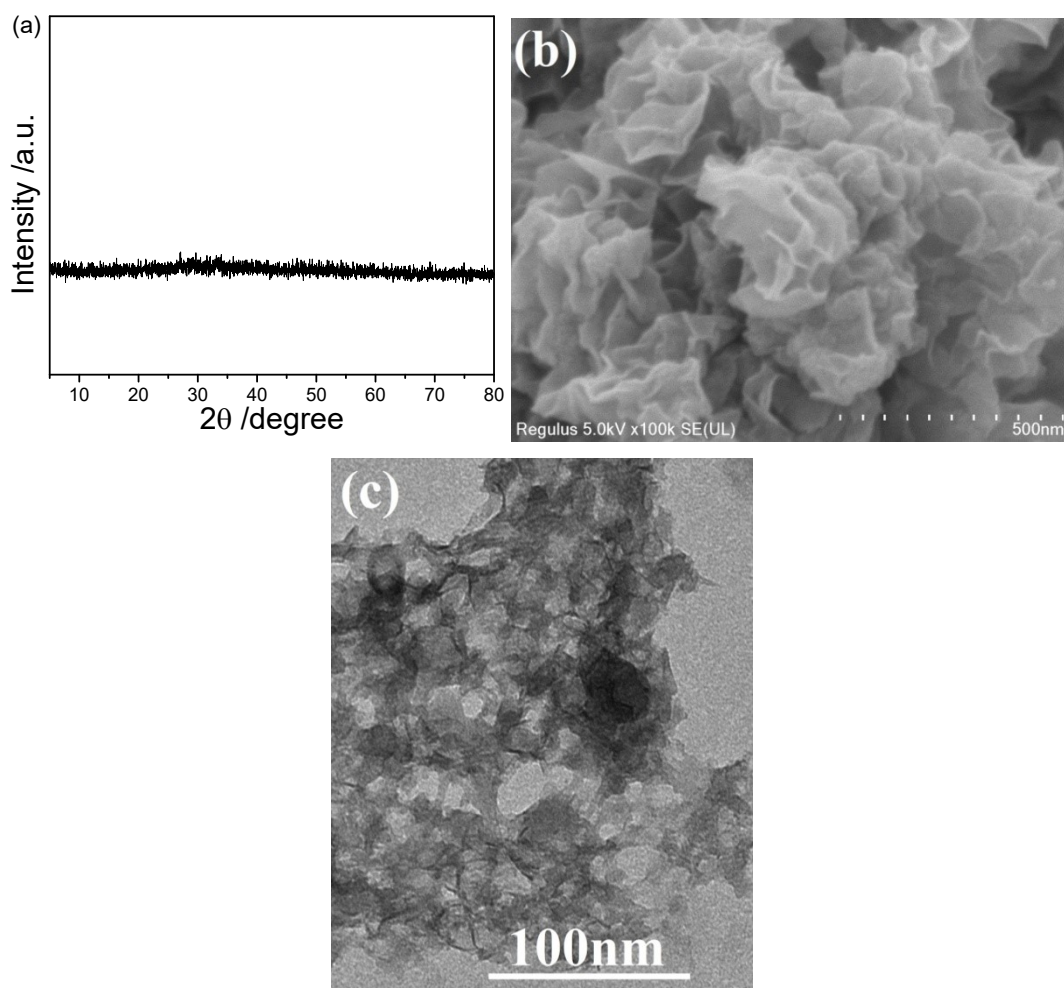
Figure S2. (a) XRD pattern, (b) SEM image and (c) TEM images of the as-deposited CeNiS on the bare NF.
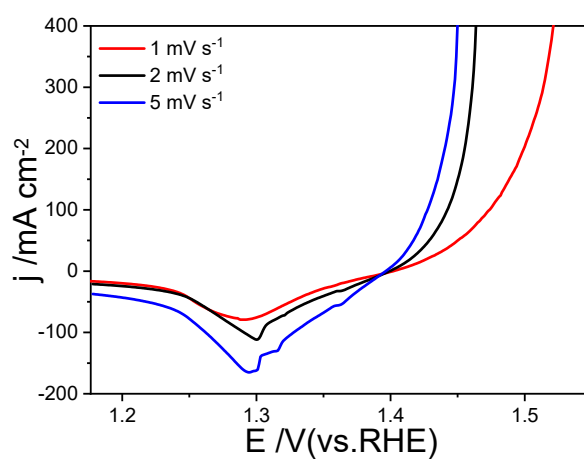
Figure S3. The LSV curves of the as-constructed CeNiS@NiMoO$_4$/NF electrode in 1 M KOH solution at the scan rates of 1, 2 and 5 mV s^{-1}, respectively.
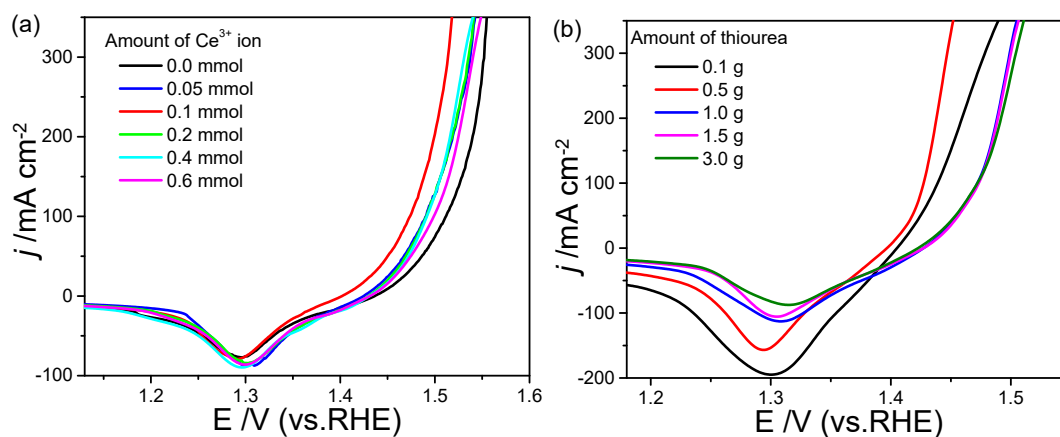
Figure S4. LSV curves of the final products deposited from the systems with various Ce^{3+} ion amounts (a) different thiourea amounts (b), respectively.
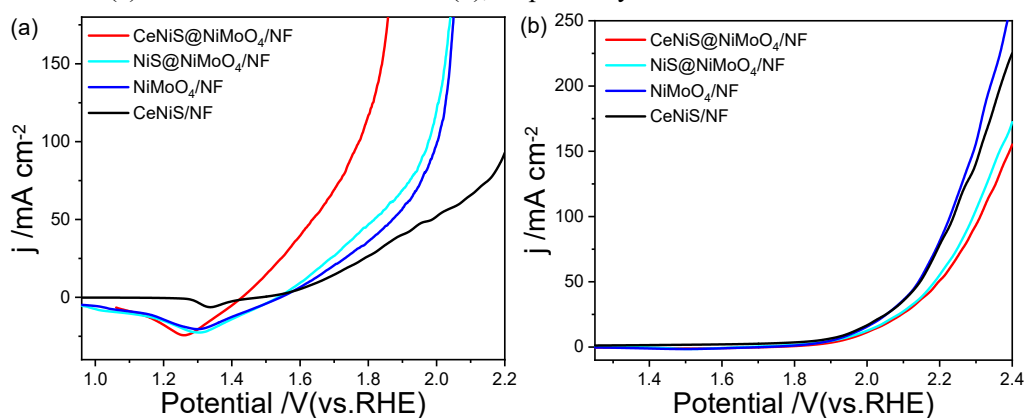
Figure S5. The polarization curves of various electrodes in 0.1 M KOH solution (a) and 0.2 M PBS (b).
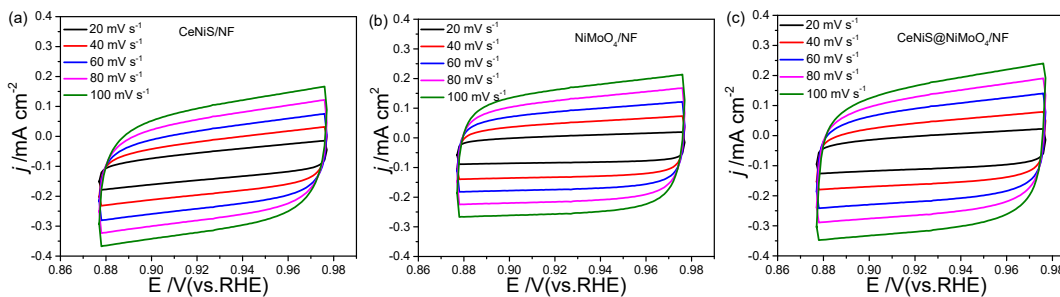
Figure S6. CV curves of the CeNiS/NF (a), NiMoO$_4$/NF (b) and CeNiS@NiMoO$_4$/NF (c) electrodes in the potential window of $0.877 \sim 0.977$ V (vs. RHE) at the scan rates of 20, 40, 60, 80, 100 mV s^{-1}.
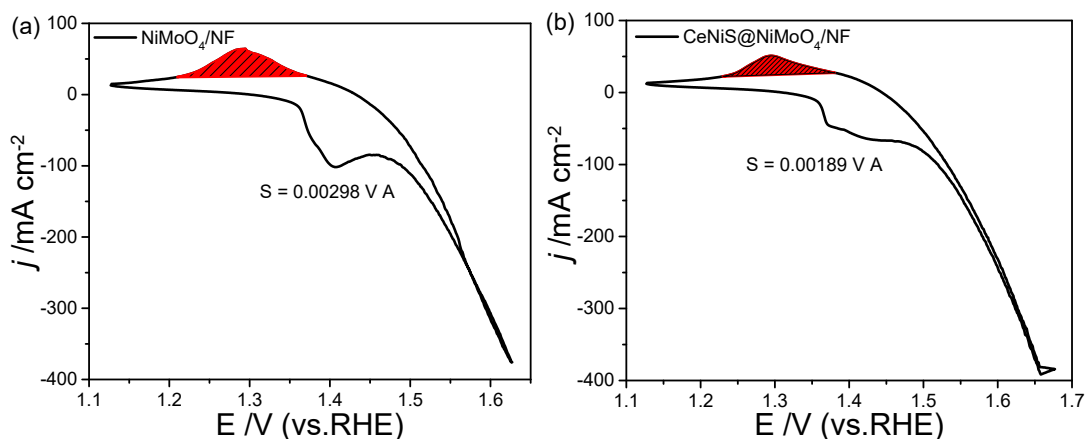
Figure S7. CV curves of the $NiMoO_4$/NF and the CeNiS@$NiMoO_4$/NF electrodes at the scan rate of 1 mV s^{-1}.
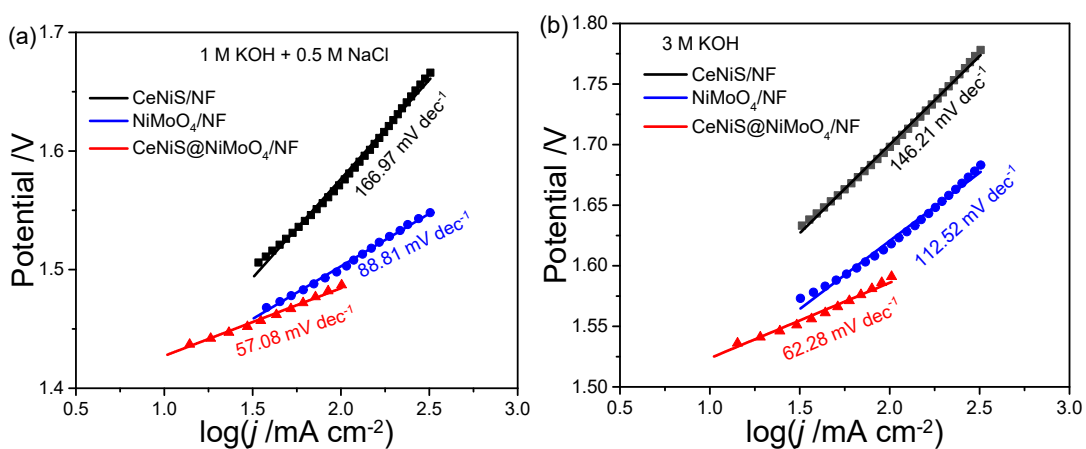
Figure S8. Tafel plots of the CeNiS/NF, $NiMoO_4$/NF and CeNiS@$NiMoO_4$/NF electrodes in different electrolytes: (a) 1 M KOH + 0.5 M NaCl saline-alkaline solution; (b) 3 M KOH solution.
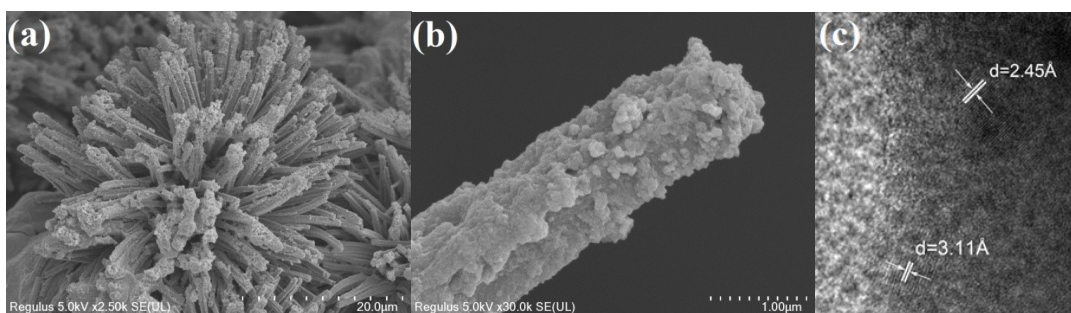
Figure S9. Electron micrographs of the catalyst after 5000 CV cycles: (a) Low magnification FESEM, (b) high magnification FESEM and (c) HRTEM images.
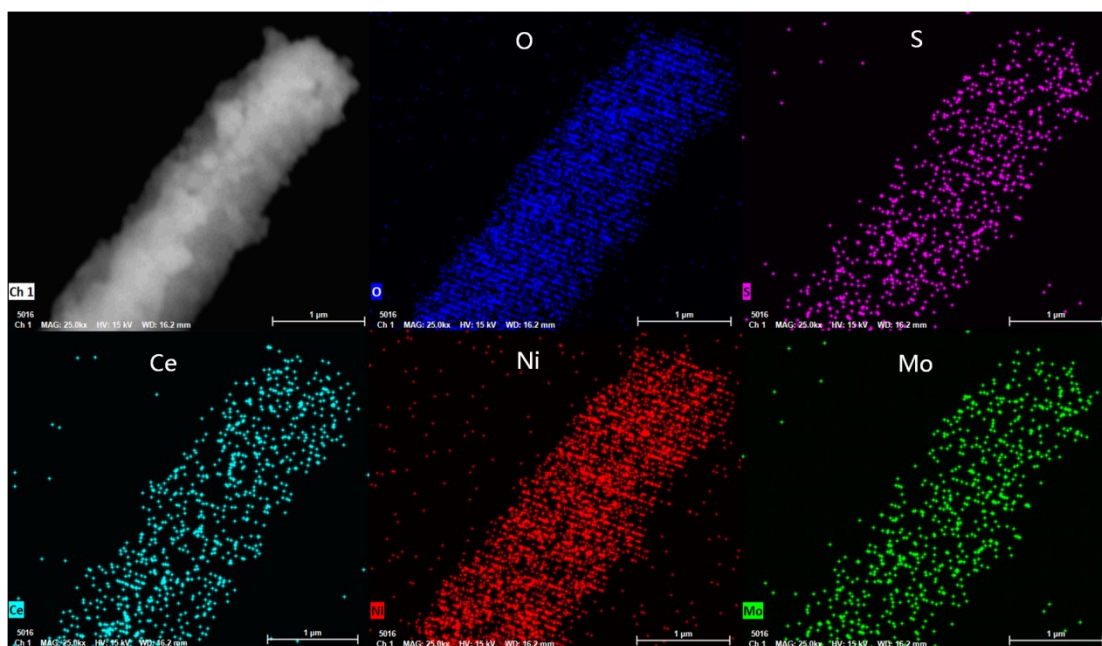
Figure S10. (a) Elemental EDS mappings of the catalyst after 5000 CV cycles.

Table S1. The loading amounts of the CeNiS, NiMoO$_4$ and CeNiS@NiMoO$_4$ on NF substrate.

Catalyst	Loading amount on NF /mg cm^{-2}
CeNiS	10.9
NiMoO$_4$	63.8
CeNiS@NiMoO$_4$	69.6

Table S2. The ICP-MS results of the as-prepared CeNiS@NiMoO$_4$ catalyst.

Element	Mass ratio /mg kg^{-1}	mol/kg
Ce	19308.2	0.1378
Mo	331136.5	3.4515
Ni	308843.1	5.262
S	4828.9	0.1506

Table S3. Comparison of overpotentials and Tafel slopes of various catalysts.

Catalyst	η_{10}(mV)	η_{50}(mV)	η_{100}(mV)	Tafel plots (mV dec^{-1})
CeNiS@NiMoO$_4$/NF	187	220	244	35.28
NiS@NiMoO$_4$/NF	221	256	282	63.16
NiMoO$_4$/NF	221	256	285	67.38
CeNiS/NF	264	346	400	196.67
IrO$_2$/NF	287	325	350	62.52

Table S4. The solution resistance (R_s) and charge transfer resistance (R_{ct}) comparison of the CeNiS/NF, NiMoO$_4$/NF and CeNiS@NiMoO$_4$/NF electrodes.

Electrode	R_s	R_{ct}
CeNiS/NF	1.56	23.19
NiMoO$_4$/NF	1.473	1.311
CeNiS@NiMoO$_4$/NF	1.431	0.8522

Table S5. Comparisons of the OER catalytic performances of the present CeNiS@NiMoO$_4$/NF catalyst with some latest non-precious metal-based electrocatalysts in 1 M KOH electrolyte.

Catalyst	Current density /mA cm^{-2}	Overpotential /mV	Tafel slope /mV dec^{-1}	Ref.
Mo-FeS NSs	10	210	50	4
RuO$_2$@Ru/RuO$_2$	10	172	53.5	5
Ni-BDC/CNF	10	221	59.6	6
MoO$_{2-x + OH-}$	10	296	45	7
NiO/NiCo$_2$O$_4$	10	357	85.4	8
Ce$_1$-CoP	10	270	63	9
np-CeO$_2$/TM	10	279	47	10
HP Ni-P	10	279	44	11
Mo$_{0.29}$Co$_{0.71}$P$_2$/MWCNTs	10	220	77.3	12
MoS$_2$-NiS$_2$/G	10	320	82	13
Ni$_3$S$_2$-1	10	280	132	14
NiO/CeO$_2$ HSs	10	265	38	15
NiMoFe@NC700	10	288	65	16
CeO$_2$@Co$_2$N	10	219	33	17
Se-(NiCo)Sx/(OH)x	10	155	87.3	18
CS-NiFeCu	10	180	33	19
CeNiS@NiMoO$_4$/NF	10	187	35.28	This work

Table S6. The ICP-MS results of the as-prepared CeNiS@NiMoO$_4$ catalyst after 5000 CV cycles.

Element	Mass ratio /mg kg^{-1}	Molar ratio /mol kg^{-1}
Ce	4184.2	0.0299
Mo	5525.1	0.0575
Ni	584667.4	9.9568
S	104.1	0.0033
K	1651.9	0.0422

Table S7. The surface compositions of various elements calculated based on the XPS spectra before and after 5000 CV cycles.

	Element	Before CV cycles	After 5000 CV cycles
Mo 3d	$3d_{5/2}$ (%)	94.42	92.84
	$3d_{3/2}$ (%)	5.58	7.16
Ce 3d	Ce^{3+} (%)	15.92	0
	Ce^{4+} (%)	84.08	100.0
Ni 2p	Ni^{2+} (%)	71.78	61.86
	Ni^{3+} (%)	28.22	38.14
O 1s	M-O (%)	47.24	18.93
	Oxygen vacancy (%)	31.35	34.85
	Adsorbed water (%)	21.41	/
	M-OH (%)	/	46.22
S 2p	$2p_{3/2}$ (%)	73.93	69.08
	$2p_{1/2}$ (%)	14.26	13.24
	SO_4^{2-} (%)	11.81	17.68

References:

1   S. Anantharaj, S. Kundu, ACS Energy Lett. 2019, 4, 1260–1264.

2   R. Farhat, J. Dhainy, L. I. Halaoui, ACS Catal. 2020, 10, 20–35.

3   L. Trotochaud, S. L. Young, J. K. Ranney, S. W. Boettcher, J. Am. Chem. Soc. 2014, 136, 6744–6753.

4   Z. Shao, H. Meng, J. Sun, N. Guo, H. Xue, K. Huang, F. He, F. Li, Q. Wang, ACS Appl. Mater. Interfaces. 2020, 12, 51846–51853.

5   Z. Wang, B. Xiao, Z. Lin, S. Shen, A. Xu, Z. Du, Y. Chen, W. Zhong, J. Energy Chem. 2021, 54, 510–518.

6   C. Qiang, M. Liu, L. Zhang, Z. Chen, Z. Fang, Inorg. Chem. 2021, 60, 3439–3446.

7   P. Guha, B. Mohanty, R. Thapa, R. M. Kadam, P. V. Satyam, B. K. Jena, ACS Appl. Energy Mater. 2020, 3, 5208–5218.

8   Z. Zhang, X. Liang, J. Li, J. Qian, Y. Liu, S. Yang, Y. Wang, D. Gao, D. Xue, ACS Appl. Mater. Interfaces. 2020, 12, 21661–21669.

9   J. Li, S. Zou, X. Liu, Y. Lu, D. Dong, ACS Sustain. Chem. Eng. 2020, 8, 10009–10016.

10   Y. Ji, J. Liu, S. Hao, Y. Xiao, L. Li, X. Liu, Inorg. Chem. Front. 2020, 7, 2533–2537.

11   D. H. Song, D. Hong, Y. K. Kwon, H. W. Kim, J. Shin, J. Shin, H. M. Lee, E. A. Cho, J. Mater. Chem. A. 2020, 8, 12069–12079.

12   A. Wang, X. Chen, L. Cheng, X. Shen, W. Zhu, L. Li, J. Pang, J. Mater. Chem. A. 2020, 8, 17621–17633.

13   S. P. Lonkar, V. V. Pillai, S. M. Alhassan, Mater. Adv. 2020, 1, 794–803.

14   X. Lv, P. Kannan, S. Ji, X. Wang, H. Wang, CrystEngComm. 2020, 22, 6517–6528.

15   Y. Zhang, F. Ye, W. D. Z. Li, Chem. Eur. J. 2021, 27, 3766–3771.

16   Z. Yu, T. Lin, C. Zhu, J. Li, X. Luo, ChemElectroChem. 2021, 8, 1316–1321.

17   J. Zhang, W. He, H. B. Aiyappa, T. Quast, S. Dieckhöfer, D. Öhl, J. R. C. Junqueira, Y. T.

Chen, J. Masa, W. Schuhmann, Adv. Mater. Interfaces. 2021, 8, 2100041.

18   C. Hu, L. Zhang, Z.J. Zhao, A. Li, X. Chang, J. Gong, Adv. Mater. 2018, 30, 1705538.

19   P. Zhang, L. Li, D. Nordlund, H. Chen, L. Fan, B. Zhang, X. Sheng, Q. Daniel, L. Sun, Nat. Commun. 2018, 9, 381.